Appl. Phys. A (2014) 116:545–554
DOI 10.1007/s00339-014-8530-0

Applied Physics A
Materials Science & Processing

RAPID COMMUNICATION

Metastable carbon allotropes in picosecond-laser-modified diamond

Sergei M. Pimenov · Andrey A. Khomich · Igor I. Vlasov · Evgeny V. Zavedeev · Alexander V. Khomich · Beat Neuenschwander · Beat Jäggi · Valerio Romano

Received: 16 May 2014 / Accepted: 19 May 2014 / Published online: 4 June 2014

Abstract In this paper, we report on the bulk modifications of type IIa single-crystal diamond with visible 10-ps pulses (at $\lambda = 532$ nm) and microstructural changes characterized by the appearance of several 'unidentifiable' vibrational modes in the frequency range of 1000–1400 cm^{-1} in the Raman spectra of laser-modified diamond. It is found that the new Raman modes are strongly pronounced in the spectra of high-stress regions in immediate proximity to the bulk microstructures in the absence of the G mode at $\sim$1580 cm^{-1} characteristic of the sp^2 phase. The high internal stresses are determined from the splitting of the triply degenerate diamond Raman line. The revealed structure transformation is localized within a narrow bulk layer near the bulk microstructures formed, and the stress relaxation is found to result in disappearance of the detected vibrational modes in the spectra. It is suggested that the formation of bulk regions with a sp^3 carbon structure consisting of Z-carbon and hexagonal diamond is responsible for the appearance of new Raman modes in the spectra of laser-modified diamond. These findings evidence that the stress-assisted formation of novel metastable carbon phases or defect structures occur in the course of bulk modification of diamond with ps-laser pulses. In addition, we report the results of simulations of internal stresses in the system 'graphitized cylinder-in-diamond' to show (1) the effect of the mechanical properties of laser-modified diamond on the resulting stresses and (2) formation of bulk microscopic regions with high stresses of >10 GPa, i.e., the conditions at which various sp^3 carbon allotropes and defect structures become more stable than graphite.

S. M. Pimenov (✉) · A. A. Khomich · I. I. Vlasov · E. V. Zavedeev
General Physics Institute, 119991 Moscow, Russia
e-mail: pimenov@nsc.gpi.ru

A. A. Khomich · A. V. Khomich
Institute of Radio Engineering and Electronics, 141190 Fryazino, Moscow Region, Russia

B. Neuenschwander · B. Jäggi · V. Romano
Bern University of Applied Sciences, Engineering and Information Technology, 3400 Burgdorf, Switzerland

1 Introduction

Since the first theoretical papers on laser-induced ultrafast phase transitions in carbon [1, 2], bulk graphitization of diamond with ultrashort pulse (femtosecond and picosecond) lasers is of permanent interest. In early experimental works, basic mechanisms of the bulk damage (graphitization) of diamond with fs- and ps-laser pulses were studied [3–5], while one of highly promising applications of micron-sized bulk modifications for diamond gem marking was found, unexpectedly, to be 'an unlikely application' because of the statistical nature of the fs-laser damage in the bulk of diamond crystals [5]. Further experimental studies have demonstrated high potential of ultrashort pulse lasers for three-dimensional (3D) bulk graphitization/microstructuring of high-quality single-crystal diamonds [6–16]. Particular applications of 3D microstructuring are related to (1) fabrication of periodic metallo-dielectric structures in single-crystal diamond, which act as a photonic crystal in terahertz region [7], and (2) fabrication of 3D graphitic electrodes for diamond radiation detectors [14–16].

As was discussed [17], there are no principal limits for graphitization of defect-free regions to occur in the bulk of diamond, when the graphitization can be considered as a

laser-stimulated process of a 'graphite-in-diamond' defect formation or amorphization of the original crystal lattice. There is, however, one fundamental point, dealing with generation of high internal stresses in the course of graphitization, which may strongly influence the phase transition and the resulting structure of laser-modified regions in the bulk of diamond. Data of the effect of high stresses on the structure and properties of laser-produced bulk microstructures in diamond are very limited, which results mainly from experimental difficulties in examination of microscopic regions in the bulk of the crystals. Previous Raman spectroscopy studies of bulk microstructures have evidenced the diamond transformation to amorphous carbon and graphitic phases [6, 7, 9, 12, 13], and measurements of the electrical conductivity showed it to be three orders of magnitude lower than that of graphite [6, 7, 11]. Modeling of internal stresses generated in diamond as a result of bulk modifications showed that the transformation of diamond to hard amorphous carbon led to much higher internal stresses (of $\sim$30 GPa) than its transformation to a soft graphitic material which, in turn, could qualitatively account for the observed 'explosive-like' damage in diamond during ps-laser bulk microstructuring [13]. In addition, recent findings of (1) crystallographic-plane-dependent character of the structural modifications and (2) formation/generation of defect centers during bulk microstructuring with ultrashort pulses should be emphasized [12, 13, 18]. The effect of crystallographic orientation is manifested in the fact that the laser-induced phase transformations are initiated along {111} planes characterized by the lowest strength in diamond [19], while the laser-induced generation of defect centers (3H, NV) is proved as the appearance/enhancement of the characteristic lines in photoluminescence (PL) spectra of diamond [12, 18]. These findings seem to be important for an insight into the mechanism of bulk modifications of single-crystal diamond with ultrashort laser pulses.

The theoretical analysis of ultrafast nonthermal phase transitions in diamond [1, 2] had showed that the laser-induced graphitization occurred within a timescale of 100 fs, with the graphitic structure remaining intact within 5 ps (maximum simulation time), while it could not describe the structure formed upon further (or full) relaxation of the laser-excited and laser-modified diamond. At the same time, it is known that graphite undergoes a phase transition to a superhard sp^3 phase [20, 21] at ambient (low) temperatures and high pressures in the range of 10–20 GPa; recent theoretical studies have revealed a variety of sp^3 carbon structures (M-carbon, W-carbon, Z-carbon, and other allotropes), which are more stable than graphite in the range of 10–20 GPa [21–26]. Such kind of low-energy sp^3 carbon structures can, in principle, be formed in/around bulk microstructures where the conditions suitable for a 'graphite-to-sp^3 carbon' phase transition can be achieved in the course of ps-laser bulk modifications of single-crystal diamond. It is the probable formation of novel (theoretically predicted) sp^3 carbon phases and/or defect structures in picosecond-laser-graphitized diamond, which is the main question to be addressed in this paper in an attempt to explain the origin of new vibrational modes revealed in the Raman spectra of the laser-modified diamond.

In this paper, we report on the bulk modifications of single-crystal diamond with visible 10-ps pulses (at $\lambda = 532$ nm) and microstructural changes characterized by the appearance of several 'unidentifiable' vibrational modes in the frequency range of 1000–1400 cm^{-1} in the Raman spectra of laser-modified diamond. The correlation of these new Raman modes with high internal stresses, also determined from the Raman spectra (from splitting of the triply degenerate Raman line in diamond), and their metastable behavior are discussed. In addition, we report the results of simulations of internal stresses in the system 'graphitized cylinder-in-diamond' to show (1) the effect of the mechanical properties of laser-modified diamond on the resulting internal stresses and (2) formation of bulk microscopic regions with high stresses of >10 GPa (i.e., the conditions at which various sp^3 carbon allotropes and defect structures become more stable than graphite [21–23, 26]).

2 Experimental details

The bulk modification/microstructuring of diamond was carried out using a picosecond MOPA (master-oscillator power-amplifier) laser system—the DUETTO^{TM} system [27, 28]. This laser system generates pulses of 10-ps duration, the repetition rate can be varied between 50 kHz and 1 MHz, and the maximum average power is 10 W.

Type IIa CVD single-crystal diamond plates of 6.0 mm × 1.34 mm × 1.26 mm size (length × width × thickness), with mechanically polished {100} growth faces and {110} side faces, nitrogen content [N] <1 ppm (from Element Six Ltd [29]), were used as the samples for ps-laser microstructuring. The CVD diamond single crystals are characterized by high crystalline and optical quality [30, 31].

The experimental setup for ps-laser bulk microstructuring is described elsewhere [12, 18]. As a laser source, we used the second laser harmonic of the DUETTO system, which generates 10-ps pulses at the wavelength $\lambda = 532$ nm. The laser pulse energy was in the range of $\varepsilon = 0.5$ μJ to $\varepsilon = 2$ μJ; the pulse repetition rate was $f = 50$ kHz. A laser beam was focused using a galvo scanner equipped with a 100-mm f–θ objective, the laser beam radius in the focal plane of the objective was

$w_o = 7$ μm. A video imaging system (model 'Digital viewer GE-5') was applied for real-time observation of the appearance and growth of a laser-graphitized region in the bulk of diamond in the course of multipulse irradiation, as described and demonstrated elsewhere [12]. In the experiments, the laser beam was incident normally to the (110) face and focused through a diamond plate to the rear side of the plate. The sample translation velocity (in the direction of a laser beam) was $V_z = 0$, i.e., the focus position was fixed, so the growth of a bulk 'graphitized' microstructure from the rear side toward the laser beam was governed by the dielectric breakdown mechanism, as was recently confirmed [18]. Focusing the laser beam to the backside interface enables us to have access [from the back side (BS) of the diamond plate] to the laser-modified diamond for structural investigations using Raman and PL spectroscopy techniques.

Figure 1 shows an optical microscopy image of bulk microstructures fabricated in a 1.34-mm-thick diamond plate by 10-ps pulses of different energies $\varepsilon = 1.6$, 1.8, and 2.0 μJ at $f = 50$ kHz. The top of the image corresponds to the BS of the plate, and bulk regions of each microstructure from the BS to a depth of about 270 μm are shown. The bulk microstructures presented in Fig. 1 are three of ten microstructures, which were considered in the analysis of the mechanism of ps-laser optical breakdown and structure growth in our recent paper [18]. Hereinafter, these microstructures are referred to as S8, S9, and S10, respectively, among which the S9 was mostly used in the Raman spectroscopy studies.

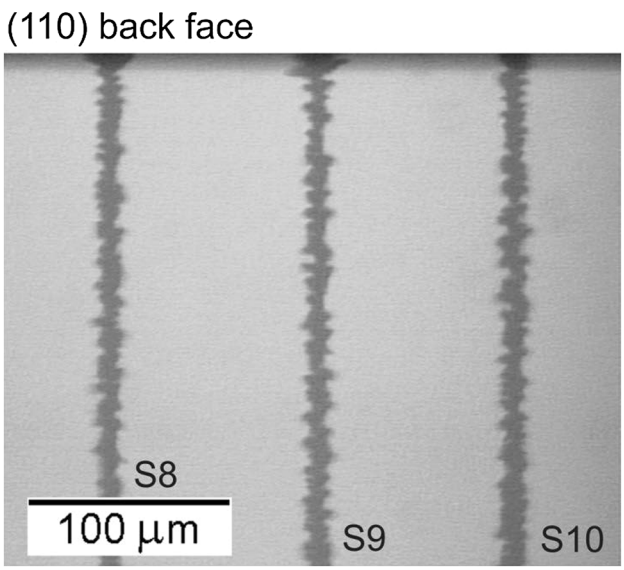

Fig. 1 Optical image of bulk microstructures fabricated in a 1.34-μm-thick diamond plate by ps-laser irradiation ($\lambda = 532$ nm, $\tau = 10$ ps) at different pulse energies $\varepsilon = 1.6$, 1.8 and 2.0 μJ from *left* to *right* (the structures are called as S8, S9, and S10, respectively), $f = 50$ kHz, $V_z = 0$; the laser beam incidence along [110] direction

The morphology of laser spots on the BS of the diamond plate was measured with a 3D surface profiler 'Zygo' (model New View 5000). The microstructural properties of laser-modified regions were examined with micro-Raman and PL spectroscopy techniques at 488 nm excitation wavelength using a Horiba Jobin–Yvon LabRAM HR800 spectrometer. Raman and PL spectra (with 0.6 and 1.8 cm^{-1} spectral resolution, respectively) were measured mainly on the BS surface of the plates at different distances and coordinates from the center of laser spots. The laser light was focused onto the surface (or into the bulk) in a spot of 1 μm diameter; the spectra were recorded at room temperature. Few Raman measurements were carried out in the confocal geometry to probe the structure S10 located at ~70 μm depth from the surface of the side (100) face, i.e., the 488-nm laser beam was focused through the side (100) face into the bulk to a depth of ~70 μm. For the excitation wavelength $\lambda_{exc} = 488$ nm and laser spot size of $d_{exc} = 1$ μm, the confocal parameter in diamond is equal to $b = 2z_R = 2n[\pi(d_{exc}/2)^2]/\lambda_{exc} = 7.7$ μm (for the Gaussian laser beam), where $z_R$is the Rayleigh length and $n = 2.4$ is the refractive index of diamond. In our Raman/PL measurements, a pinhole of 50 to 300 μm diameter was placed at the back focal plane of a 100× objective (to reduce the effective sampling volume), so the confocal parameter was in the range from ~4 to 6 μm.

3 Results

3.1 Detection of new Raman modes in laser-modified single-crystal diamond

PL and Raman spectra measured on the (110) back face in different points within and outside the microstructure S9 are displayed in Fig. 2. Figure 2a shows an optical transmission image of the S9, and the directions *X* and *Y* along which the PL/Raman measurements were made. The *X*-axis is directed normally to the (100) side face toward the center of the 1.26-mm-wide plate, and the *Y*-axis is parallel to the (100) side face and is directed along the BS surface from the S9 to the S8 microstructure (shown in Fig. 1).

Figure 2b shows characteristic features in the PL spectra recorded (1) in the center of the laser spot formed at the (110) back face surface during the S9 microstructure fabrication, (2) in close proximity to the laser spot at 10 μm distance from the center, and (3) far away from the laser spot (at 150 μm distance), i.e., location equivalent to the original diamond. PL spectra were measured in the range of 490–800 nm. The PL spectrum of the original crystal is dominated by an intensive Raman line at 522 nm and a weak NV luminescence [32] at wavelengths of 570–800 nm. The Raman spectrum (not shown here) is

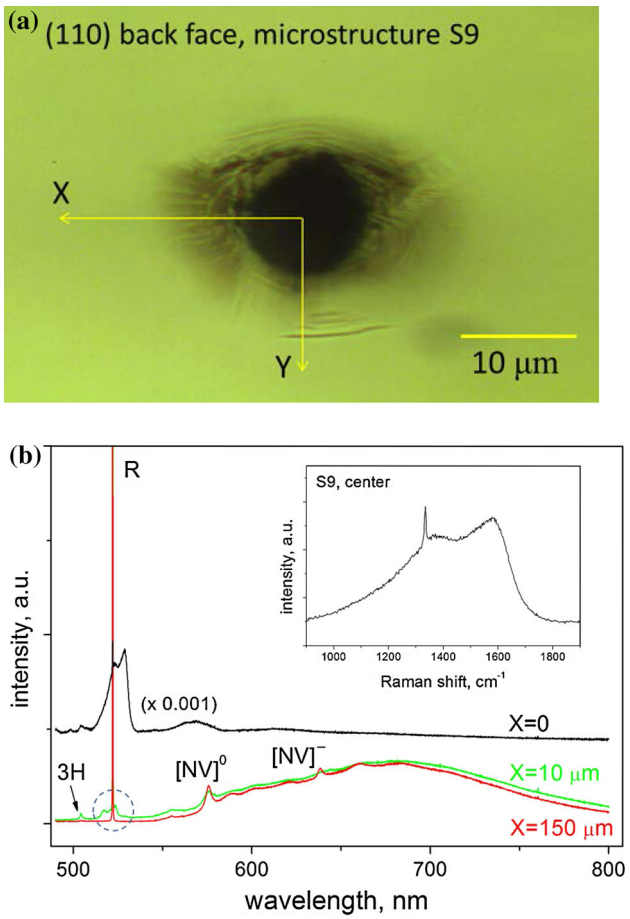

Fig. 2 **a** Optical transmission image of the microstructure S9 (viewed from the (110) back face) examined with PL/Raman spectroscopy at varying distances from the S9 center along the X and Y directions at the (110) back face surface; **b** PL spectra measured in the center of the S9 (Raman spectrum—in the *inset*) and along the X-axis at $X = 10$ μm and $X = 150$ μm, excitation wavelength 488 nm; R is the diamond Raman line at 522 nm, new Raman modes are marked by a *dashed circle* (see text for details)

characterized by the first-order Raman line at $\omega_{\text{diam}} = 1332.5\ \text{cm}^{-1}$ (full width half maximum (FWHM) $= 1.75\ \text{cm}^{-1}$), evidencing a high-structural quality of the original single-crystal diamond.

In the spot center of the S9, the Raman spectrum is dominated by two broad bands at $\omega_{\text{D}} = 1350\ \text{cm}^{-1}$ (D band) and $\omega_{\text{G}} = 1580\ \text{cm}^{-1}$ (G band) which are typical of amorphous carbon structures, particularly tetrahedral amorphous carbon (ta-C) films with high sp^3 content [33], as was discussed in our previous papers [12, 13]. A weak first-order diamond Raman peak shifted to a higher frequency of $\sim 1334\ \text{cm}^{-1}$ is also observed in the spectrum, indicating a composite 'diamond-amorphous carbon' structure of the laser-modified diamond.

Examination of the local PL behavior with increasing distance from the spot center has revealed the appearance of new vibrational modes in close vicinity to the diamond Raman line. The discovered Raman modes are marked by a dashed circle in Fig. 2b and are displayed in more detail in Fig. 3. These Raman bands (of intensity almost two orders of magnitude lower than that of the diamond Raman line) are positioned in the frequency range of 1000–1400 cm^{-1}. It should be also mentioned that under the given bulk microstructuring conditions ([110] beam direction, pulse repetition rate $f = 50$ kHz), the 3H luminescence at 504 nm was observed to be much weaker than that in the previous experiments with 10-ps pulses under the [100] laser beam incidence and $f = 10$ kHz [12].

The observed transformations in the Raman spectra measured along the X direction (see laser spot in Fig. 2a) are shown in Fig. 3a and those measured along the Y direction are shown in Fig. 3b; the spectra in Fig. 3b were recorded at higher resolution due to larger integration time. It is interesting to see that the 'amorphous carbon' structure inside the laser spot of radius $R = w_0 = 7$ μm (i.e., inside the microstructure S9) is transformed into a new carbon phase located within a narrow bulk layer [8 μm $< X(Y) <$ 12 μm] surrounding the structure S9. In addition to the spatial localization, this 'unidentifiable' carbon phase and/or defect structure is characterized by four Raman modes ($\omega_1 \approx 1020\ \text{cm}^{-1}$, $\omega_2 \approx 1120\ \text{cm}^{-1}$, $\omega_3 \approx 1160\ \text{cm}^{-1}$, and $\omega_4 \approx 1280\ \text{cm}^{-1}$) at frequencies lower than the diamond phonon frequency $\omega_{\text{diam}} = 1332.5\ \text{cm}^{-1}$ and one mode $\omega_5 \approx 1390\ \text{cm}^{-1}$ at higher frequency. At distances $X > 14$ μm, only the first-order diamond Raman line is present in the spectra obtained. The Raman spectra–on–distance dependence correlates qualitatively with the optical images of the microstructure S9 (both in Figs. 1, 2a) where bulk regions of lower transmission evidence the presence of non-diamond phases and its spatial non-uniformity reflects a crystallographic-plane-dependent character of the bulk modifications as discussed elsewhere [12, 18].

The above carbon phase was found not only in the near-surface micrometer thick layers at the (110) back face of the crystal but also in the bulk regions neighboring to the S10 microstructure at a depth of ~ 200 μm from the (110) back face surface. For this, Raman measurements were made in the confocal geometry to probe the structure S10 located at ≈ 70 μm depth from the surface of the side (100) face. Figure 3c compares the Raman spectra of the S9 and S10 microstructures and shows the presence of the identical Raman modes in the spectra, except for smearing of the ω_5 and ω_{G} bands. A reason of smearing of the Raman bands is due to the dimensions of the bulk region probed. During the measurements, the confocal parameter is ~ 4 μm, and a microscopic volume of about 1 $\mu\text{m}^2 \times 4$ μm is probed in the direction normal to the S10 structure, leading to superposition of changing Raman bands from different bulk microregions and smearing of the spectral bands. Note that similar Raman spectra were recently

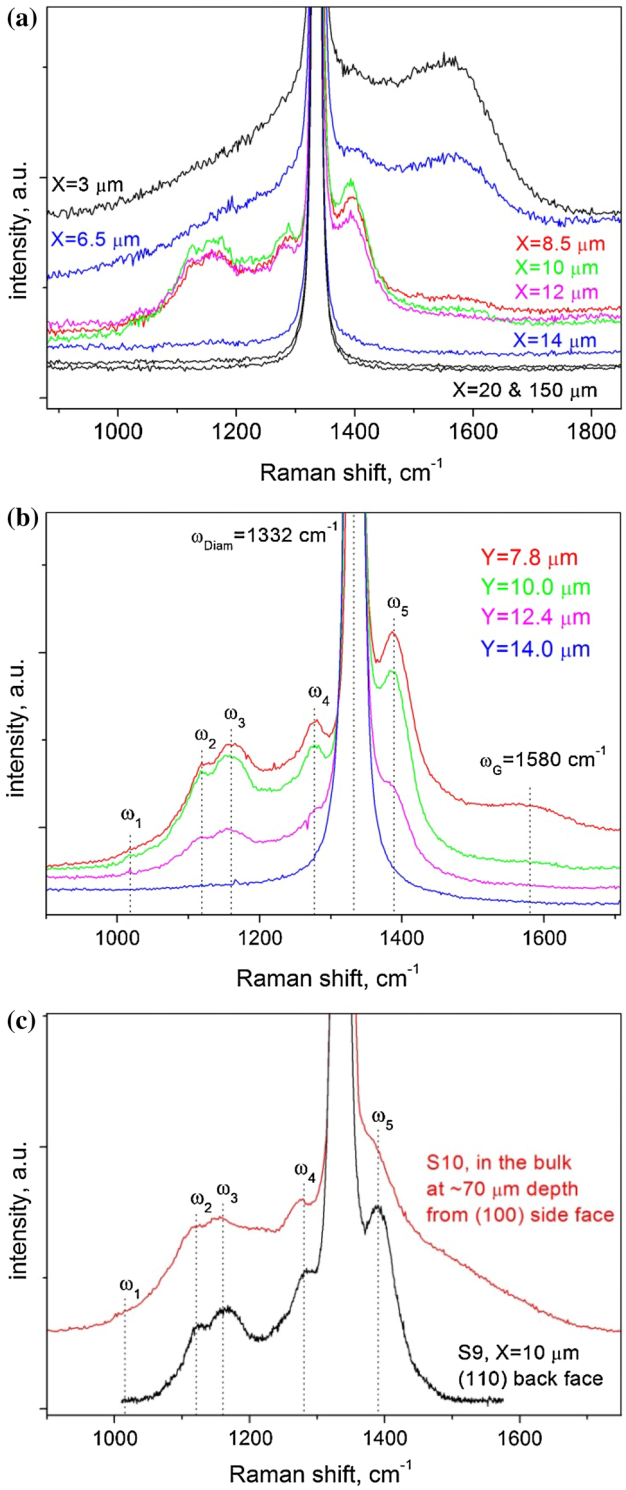

◀**Fig. 3** **a** Raman spectra of the S9 microstructure measured at varying distances from the center along the X direction (in Fig. 2a), two spectra at $X = 3$ μm and $X = 6.5$ μm are shifted upwards for clarity; **b** Raman spectra measured at varying distances along the Y direction (in Fig. 2a), **c** Raman spectrum of the S10 microstructure measured in the bulk at ≈70 μm depth from the surface of the side (100) face in comparison with the spectrum of the S9 structure measured at $X = 10$ μm. The frequencies of the new Raman modes are $\omega_1 \approx 1020$ cm^{-1}, $\omega_2 \approx 1120$ cm^{-1}, $\omega_3 \approx 1160$ cm^{-1}, $\omega_4 \approx 1280$ cm^{-1}, and $\omega_5 \approx 1390$ cm^{-1}

reported for a bulk microstructure fabricated in diamond (to a depth of ∼30 μm) by laser irradiation with 1-ps pulses [34].

We emphasize briefly some distinctive features of the detected Raman modes (ω_1, ω_2,…, ω_5) in the spectra of the laser-modified diamond. First, the intensities of these modes change 'synchronously' (see Fig. 3b), implying the content of a new carbon phase to vary with distance from a bulk microstructure. Second, the high-frequency mode at $\omega_5 \approx 1390$ cm^{-1} is different from the disorder-induced D band positioned near $\omega_D = 1350$ cm^{-1} for the excitation wavelength $\lambda_{exc} = 488$ nm [35, 36] (in spite of proximity in the positions of these modes). It should be noted that the ω_5 mode is observed in the spectra in the absence of the G band at $\omega_G \sim 1580$ cm^{-1}. Third, the new Raman modes are localized in a narrow region adjacent to the bulk microstructure where high internal stresses generated in the course of bulk graphitization can influence the final structure of laser-modified diamond. In the following Sects. (3.2 and 3.3), we analyze the results of modeling and additional Raman data on the internal stresses in laser-modified diamond before coming to our final discussion and conclusions about the origin of the new Raman modes shown in Fig. 3.

3.2 Modeling of internal stresses in the system 'graphitized cylinder-in-diamond'

Here, we consider the task of internal stresses generated in diamond as a result of bulk structure transformations and estimate the stresses in the system 'graphitized cylinder-in-diamond'. The modeling scheme for a graphitized cylinder embedded in diamond is shown in Fig. 4a. In simulations, we assume that a cylinder of radius R (infinite along Z-axis) is taken out from diamond, 'graphitized' (the ratio of expansion is the same in all axes) and then it is placed back into diamond. An objective of the modeling is to find out how the properties of laser-modified material (ρ_1, E_1, ν_1) affect the resulting internal stresses in the system (ρ_1 is the material density, E_1 is the Young's modulus, and ν_1 is the Poisson's ratio; ρ_2, E_2, ν_2 are the density, Young's modulus, and Poisson's ratio of diamond).

Using Hooke's law for isotropic materials (see, e.g., [37]) in the form in which the strain is expressed in terms of the stress tensor and assuming certain equilibrium and boundary conditions, we get the following analytical expressions for the stresses inside the graphitized cylinder

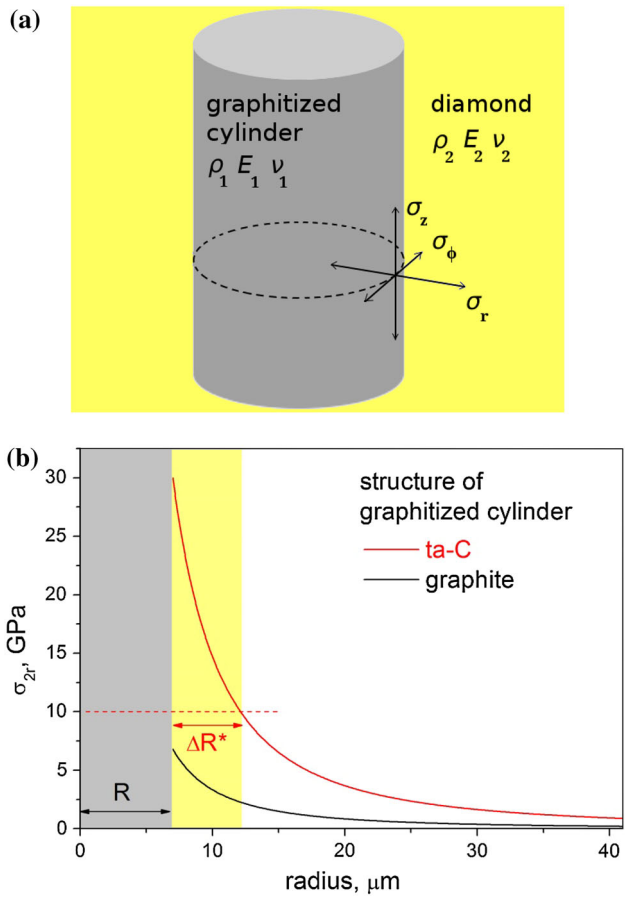

Fig. 4 **a** Scheme of modeling of internal stresses in the system 'graphitized cylinder-in-diamond'; **b** stress-on-distance dependence in diamond for two different structures (see properties of the structures in Table 1) of a graphitized cylinder of radius R, a yellow region of ΔR^* size denotes a bulk layer around the cylinder where the stresses are higher 10 GPa

$(\sigma_{1r}, \sigma_{1\phi}, \sigma_{1z})$ and in the surrounding diamond $(\sigma_{2r}, \sigma_{2\phi}, \sigma_{2z})$:

$$\sigma_{1r} = \sigma_{1\phi} = -C(1 + kv_1)E_2 = \text{const}, \quad (1)$$

$$\sigma_{1z} = -C\{[k + v_1(2 - k)]E_2 + (1 + v_2)E_1\} = \text{const}, \quad (2)$$

where $C = \dfrac{(k-1)E_1}{kE_2(1 - v_1 - 2v_1^2) + E_1(1 + v_2)}$,

$k = (\rho_2/\rho_1)^{1/3}$,

$$\sigma_{2r}(r) = -\sigma_{2\phi}(r) = \sigma_{1r}(R^2/r^2), \quad (3)$$

$$\sigma_{2z} = 0, \quad (4)$$

where R is the radius of a graphitized cylinder and r is the radial distance from the center of the cylinder.

Based on our Raman data of bulk microstructures (see [12, 13] and Fig. 2b), two types of material of the graphitized cylinder are selected in calculations using the above expressions (1)–(4). The first material is tetrahedral amorphous carbon (ta-C), which is dense and hard, with the density of $\rho_1 = 2.9$–3.1 g/cm^3 and Young's modulus $E_1 = 550$–750 GPa (see refs. [33, 38, 39]). The second material is isotropic pyrocarbon (pyrographite), which is less dense ($\rho_1 = 2.2$ g/cm^3) and soft ($E_1 = 28$ GPa) [40]. For diamond, we take: $\rho_2 = 3.5$ g/cm^3, $E_2 = 1{,}050$ GPa, $v_2 = 0.07$ [41]. The results of calculations of internal stresses are given in Table 1.

It should be noted that under the assumption of the equal expansion ratio for all axes, the compressive stresses along Z-axis and in the XY plane were found to be appreciably different (compare the $|\sigma_{1r}|$ and $|\sigma_{1z}|$ in Table 1), that is, probably not the case in real conditions when the material undergoes a structure transformation under the pressure. We therefore consider another limiting case, assuming the stresses (inside the cylinder) equal for all axes: $\sigma_{1r} = \sigma_{1\phi} = \sigma_{1z} = |\sigma_1|^*$. The obtained values of $|\sigma_1|^*$ are given in Table 1. The expressions (3)–(4) for the stresses in diamond are valid. The stress-on-radius dependences in diamond (surrounding the laser-graphitized cylinder) are displayed in Fig. 4b for both, the hard amorphous and soft graphitic materials inside the cylinder of radius $R = 7$ μm (the cylinder radius is taken equal to the laser beam radius $w_0 = 7$ μm). A region of $\Delta R^* \sim 5$ μm size (marked in Fig. 4b by yellow color) shows a bulk layer around a graphitized cylinder where the internal stresses are higher 10 GPa.

The first important result of modeling is that the transformation from diamond to hard amorphous carbon (known as the material with high sp^3 content of 80–85 % [33]) results in considerably higher internal stresses than the transformation to the soft graphitic material, though the $\Delta\rho = \rho_2 - \rho_1$ is considerably smaller. The second important result is that the high-pressure conditions are realizable, and the formation of sp^3 carbon allotropes more stable than graphite at ambient temperatures is feasible under the bulk microstructuring of diamond with ultrashort laser pulses. However, under experimental

Table 1 Stresses in a 'graphitized cylinder-in-diamond' system (shown schematically in Fig. 4a)

Material	ρ_1 (g/cm^3)	E_1 (GPa)	v_1	$\lvert\sigma_{1r}\rvert$ (GPa)	$\lvert\sigma_{1z}\rvert$ (GPa)	$\lvert\sigma_1\rvert^*$ (GPa)
ta-C 1	3.1	750	0.12	21.1	36.0	24.0
ta-C 2	3.1	550	0.12	17.7	26.9	19.6
ta-C 3	2.9	550	0.12	27.4	42.0	30.0
Isotropic pyrocarbon	2.2	28	0.2	6.7	7.4	6.8

ρ_1, E_1, v_1 are the density, Young's modulus, and Poisson's ratio of laser-modified material; $|\sigma_{1r}|$, $|\sigma_{1z}|$, and $|\sigma_1|^*$ are the stresses inside a graphitized cylinder (see text for details)

conditions, the stress distribution is different and much more complicated, resulting principally from the spatially non-uniform, crystallographic-plane-dependent character of the bulk modifications in diamond (see Fig. 1 and refs. [12, 18]).

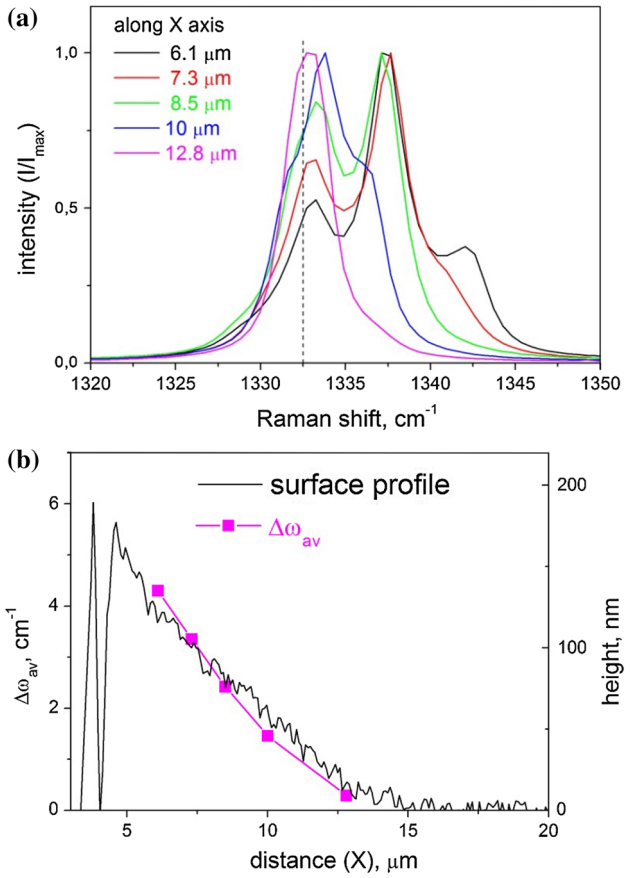

Fig. 5 **a** High-resolution Raman spectra measured along the *X*-axis (shown in Fig. 2a) at increasing distance from the S9 microstructure; **b** average frequency shift $\Delta\omega_{av}$ (for the above spectra) vs distance *X* (*solid squares*) superimposed onto the surface swelling profile measured along the *X*-axis

3.3 Stress-induced shift and splitting of the first-order Raman line in laser-modified diamond

Information on the internal stresses generated in diamond as a result of bulk modifications has been derived from the Raman spectroscopy analysis of the triply degenerate first-order diamond Raman line. It is known [42–46] that, depending on stress configurations, the diamond Raman peak can be shifted relative to the diamond phonon frequency $\omega_{diam} = 1332.5\ cm^{-1}$ and split into two or three components. The evolution of the diamond Raman spectrum measured along the *X*-axis at different distances from the S9 center (from $X = 6.1$ to 12.8 μm) is shown in Fig. 5a. The Raman measurements cover the range from the edge of the ps-laser spot ($X \approx 6$–6.5 μm) to the edge of a deformed area ($X \approx 12$–13 μm) around the ps-laser spot on the (110) back face of the diamond plate (see Fig. 2a).

It is clearly seen in Fig. 5 that the first-order Raman line is asymmetrically broadened, shifted to higher frequencies (relative to $\omega_{diam} = 1332.5\ cm^{-1}$) and split into three components. Such a behavior of the Raman spectra is due to the presence of anisotropic internal stresses in the near-surface layers. The observed splitting of the Raman line is related to a narrow region neighboring to the S9 microstructure ($X = 6$–10 μm), though the three components become less resolved in the spectrum at $X = 10$ μm. With distance, the triple degeneracy of the diamond Raman line is restored: The spectrum of $X = 12.8$ μm is represented by a single band slightly broadened and shifted upward relative to the bulk frequency, and at $X > 14$ μm, the spectrum is similar to that of the original crystal. The Raman spectra measured at four local spots, from $X = 6.1$ μm to $X = 10$ μm, are fitted with three Lorentzian peaks at frequencies of ω_{diam1}, ω_{diam2}, and ω_{diam3}; the data of the frequencies and full width at half maximum (FWHMs) of the peaks are given in Table 2. In addition, the average frequency shift $\Delta\omega_{av}$ is calculated using the following expression [46]

Table 2 Frequencies and FWHMs of the Raman lines obtained from deconvolution and Lorentzian peak fitting for the spectra in Fig. 5a compared with those of the original diamond plate

Distance along *X* (μm)	ω_{diam1}/FWHM (cm^{-1})	ω_{diam2}/FWHM (cm^{-1})	ω_{diam3}/FWHM (cm^{-1})	$\Delta\omega_{av}$ (cm^{-1})
6.1	1332.88/3.62	1337.41/2.74	1341.97/2.90	4.30
7.3	1332.96/3.61	1337.57/2.78	1340.98/2.48	3.35
8.5	1331.97/2.76	1333.53/3.09	1337.20/2.51	2.42
10	1331.53/1.94	1333.71/2.76	1336.30/2.15	1.46
12.8	1332.79/2.78			0.29
Original plate	1332.5/1.75			0

The average frequency shift $\Delta\omega_{av}$ calculated using (5) for the spectra in Fig. 5a

$$\Delta\omega_{\mathrm{av}} = \frac{\Delta\omega_1 I_1 + \Delta\omega_2 I_2 + \Delta\omega_3 I_3}{I_1 + I_2 + I_3}, \quad (5)$$

where $\Delta\omega_i = \omega_{\mathrm{diam(i)}} - \omega_{\mathrm{diam}}, (i = 1, 2, 3)$, and the I_1, I_2, and I_3 are the intensities of the corresponding Lorentzian peaks in the Raman spectra under consideration. The average frequency shift can be considered as a measure of a mean hydrostatic stress, i.e., $\Delta\omega_{av} \propto \sigma_{av}$. In Fig. 5b, the $\Delta\omega_{\mathrm{av}}$ is shown to decrease from 4.3 to 0.29 cm^{-1} with distance, correlating with the modeling results of the stress-on-radius dependence in Fig. 4b. It should be also noted that the $\Delta\omega_{\mathrm{av}}$ value is proportional to the swelling height (Δh) of the surface profile; the surface swelling is known to result from the bulk structure transformation, lower density of the laser-modified diamond, and high internal stresses in the bulk [47]. In case of hydrostatic stresses, the frequency shift of $\Delta\omega_{av} = 4.3$ cm^{-1} corresponds to the compressive stress of $\sigma_{av} = \Delta\omega_{\mathrm{av}}/a_{\mathrm{h}} = 1.6$ GPa (where $a_{\mathrm{h}} = 2.64$ cm^{-1}/GPa is the hydrostatic pressure coefficient [48]). The real stress pattern around the microstructure S9 is different from the hydrostatic conditions, and the calculated values of $\sigma_{\mathrm{av}} \propto \Delta h$ are considered as a hydrostatic component of an unknown stress distribution in the bulk near-surface regions.

The detailed analysis of a particular stress pattern is out of the goals of this paper, rather our analysis is aimed at estimation of stresses around the bulk microstructures formed. The estimation of stresses was made for the bulk regions around the S10 microstructure probed with a Raman beam in the [100] direction, i.e., in the direction perpendicular to the 'graphitic' cylinder (schematically shown in Fig. 4). The Raman spectrum measured in the bulk region near the S10 structure, at the depth of 60 μm from the (100) side face, is shown in Fig. 6. In this case, the [100]-oriented stress dominates and the coefficient $(\Delta\omega/\Delta\sigma)_{[100]} = 0.73$ cm^{-1}/GPa is used [43]. Taking $\Delta\omega_{[100]} = \omega_{\mathrm{diam2}} - \omega_{\mathrm{diam1}} = 7.8$ cm^{-1} from the spectrum in Fig. 6, we get the mean value of the compressive stress of $\sigma \sim 11$ GPa over the probed volume.

In addition, the stress relaxation in the near-surface layers was found to occur in the course of repeated measurements of the Raman spectra at $X = 10$ μm (S9 microstructure), that resulted, eventually, in disappearance of the ω_1–ω_5 modes in the spectra. The effect of the stress relaxation on the Raman spectra is shown in Fig. 7, which was observed to develop on the timescale of several months. All the spectra in Fig. 7 were measured in confocal mode except for the spectrum 1 in Fig. 7a. After deconvolution of the Raman spectra (in Fig. 7b) into three Lorentzian peaks, the calculation of the average frequency shift ($\Delta\omega_{\mathrm{av}}$) showed it to be progressively reduced during the relaxation process. It follows from Fig. 7 that a month-long stress relaxation resulted in 'self-healing' of the defect structure of diamond, which was accompanied by

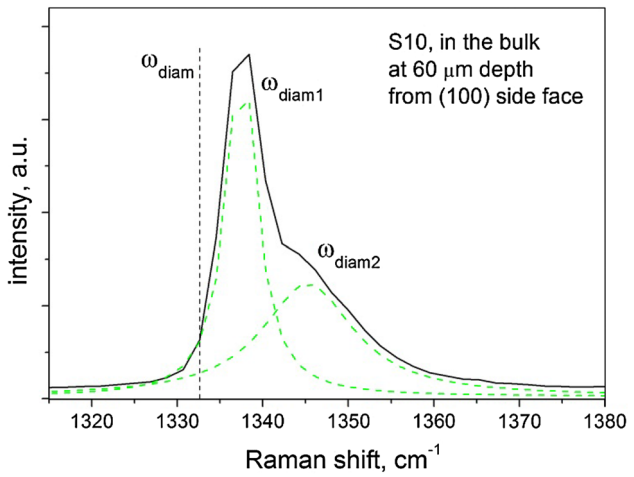

Fig. 6 Raman spectrum measured in the bulk near the S10 structure at the depth of 60 μm from the (100) side face. $\omega_{\mathrm{diam}} = 1332.5$ cm^{-1}, $\omega_{\mathrm{diam1}} = 1337.5$ cm^{-1}, $\omega_{\mathrm{diam2}} = 1345.3$ cm^{-1}

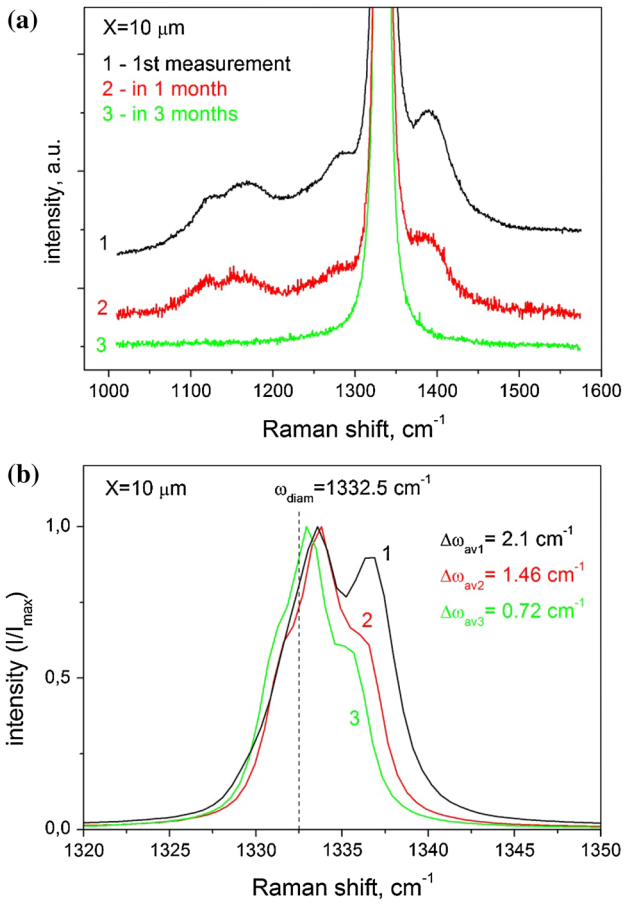

Fig. 7 Evolution of the low-intensity Raman modes (**a**) and the first-order diamond Raman line (**b**) (in the spectra of the S9 microstructure) during 4-month period: *1* first measurement, *2* in 1 month, and *3* in 3 months

disappearance of the ω_1–ω_5 modes in the Raman spectra of the laser-modified diamond.

4 Discussion and conclusive remarks

In the concluding part, we discuss and summarize the obtained results in an attempt to understand the origin of the new vibrational modes (ω_1, ω_2,…, ω_5) in the Raman spectra of the laser-modified diamond.

First, it is found that the new Raman modes are strongly pronounced in the spectra of high-stress regions in immediate proximity to the bulk microstructures in the absence of the G mode ($\omega_G \sim 1580$ cm^{-1}) characteristic of the sp^2 phase. The revealed structure transformation is localized within a narrow bulk layer near the bulk microstructures, at the distance of 8–12 μm from the center of the microstructures. It implies that a new carbon structure is formed at temperatures appreciably lower than that inside the laser-irradiated bulk regions. The detected modes ω_1–ω_5 behave 'in phase' (as shown in Fig. 3b), and their intensities are about two orders of magnitude lower than that of the diamond Raman line. This gives a rough estimate of the content of the new allotropic structure of the order of 1 % and proves that the new modes are localized in the region, which is much smaller than the volume typical of Raman probing in confocal mode (a few μm^3). Note also that the Raman band features do not conform to the phonon density of states (PDOS) [49], as opposed to the spectra of radiation-damaged diamonds after ion implantation [50, 51] or fast neutrons irradiation [52] which exhibit broad band shapes close to the PDOS of diamond.

Second, a comparison of the experimental spectra (shown in Fig. 3) was made with the calculated frequencies of the Raman modes for different sp^3 carbon allotropes, including bct-C$_4$, M-carbon, W-carbon, Z-carbon, and hexagonal diamond (HD) [24, 25]. The ω_1–ω_5 modes were found to be well fitted with the Raman modes of a sp^3 carbon structure consisting of two carbon allotropes, Z-carbon and HD, under pressure of 18–20 GPa. Particularly, the first-order Raman spectrum of Z-carbon at 18 GPa exhibits three large peaks at 1122, 1245, and 1390 cm^{-1} and one low-intensity peak at 1035 cm^{-1} (A_g modes); the spectrum of HD is characterized by the E_{2g} and E_{1g} modes at 1275 and 1385 cm^{-1}, respectively [25]. That is the presence of bulk regions with the modified structure of 'Z-carbon embedded in HD' and high stresses of 18–20 GPa can explain the appearance of the new Raman bands in the spectra.

There is an apparent discrepancy between the stress values (18–20 GPa) 'required' for the observed frequencies of the new Raman bands and the stress values (11 GPa) estimated from the splitting of the diamond Raman line in the bulk regions adjacent to the modified microstructure. The difference and 'underestimation' of the stresses is caused by the spatial resolution of the Raman technique, which is limited by the confocal parameter of several microns. At such resolution, a lower part of the stress distribution (see Fig. 4b) is well resolved, giving a high intensity and almost constant shift for the Raman lines. An upper part, localized in a layer of width <1 μm, gives an extended line shift and weaker intensity that can make the high-stressed region unresolvable in Raman spectra. This factor is especially important in case of low concentration of high-stress regions in the crystal, when the averaged stress value derived from the Raman spectra analysis is (much) lower than a local stress in a modified region. An additional evidence in favor of high internal stresses, close to the fracture strength of the material, comes from the explosive-like character of crack growth and damage observed during ps-laser bulk microstructuring of diamond [13]. Formation of microcracks could also be a reason of a month-long stress relaxation discussed above (and shown in Fig. 7).

In the Raman spectra of the S9 and S10 microstructures, the position of the new Raman bands (the ω_1–ω_5 modes) is practically not changed, whereas the position of the Raman peaks is known to be pressure dependent and to be shifted to higher or lower frequencies, depending on the stress value. The structural bulk modifications and generated stress values are controlled by laser irradiation parameters (pulse duration, laser intensity, and pulse repetition rate), so are the unchanged positions of the ω_1–ω_5 Raman bands observed for almost the same irradiations conditions during the S9 and S10 bulk microstructuring. Changing the pulse duration, we observed a shift of the Raman bands to lower frequencies by ~ 10 cm^{-1}. This is equivalent to a decrease of the stress value by ~ 3 GPa, but the resulting value of 15 GPa still remains to be higher than the calculated transition pressure of ≈ 10 GPa for Z-carbon [23].

To conclude, the appearance of new vibrational modes (ω_1, ω_2,…, ω_5) in the Raman spectra of laser-modified diamond is suggested to result from the formation of submicron bulk regions with a sp^3 carbon structure consisting of carbon allotropes, such as Z-carbon and HD. These results along with our previous findings on crystallographic-plane-dependent character of structural modifications and formation/generation of defect centers during bulk microstructuring [12, 13, 18] demonstrate that bulk modification of diamond with ultrashort pulse lasers is a promising technique to generate new carbon phases, optical centers, and ordered defect structures in single-crystal diamond.

Acknowledgments The work was partly supported by the SNSF project IZ73Z0-128088/1.

References

1. H.O. Jeschke, M.E. Garcia, K.H. Bennemann, Appl. Phys. A **69**(Suppl.), S49 (1999)
2. H.O. Jeschke, M.E. Garcia, K.H. Bennemann, Phys. Rev. B **60**, R3701 (1999)
3. S. Preuss, M. Stuke, Appl. Phys. Lett. **67**, 338 (1995)
4. A.A. Malyutin, S.V. Garnov, S.M. Pimenov, O.G. Tsarkova, V.I. Konov, SPIE **5147**, 33 (2003)
5. J.B. Ashcom, PhD thesis (Harvard University, 2003); http://mazur-www.harvard.edu/sentFiles/Mazurpubs_309.pdf
6. Y. Shimotsuma, M. Sakakura, S. Kanehira, J. Qiu, P.G. Kazansky, K. Miura, K. Fujita, K. Hirao, J. Laser Micro/Nanoeng. **1**, 181 (2006)
7. M. Shimizu, Y. Shimotsuma, M. Sakakura, T. Yuasa, H. Homma, Y. Minowa, K. Tanaka, K. Miura, K. Hirao, Opt. Express **17**, 46 (2009)
8. T.V. Kononenko, M. Meier, M.S. Komlenok, S.M. Pimenov, V. Romano, V.P. Pashinin, V.I. Konov, Appl. Phys. A **90**, 645 (2008)
9. T.V. Kononenko, M.S. Komlenok, V.P. Pashinin, S.M. Pimenov, V.I. Konov, M. Neff, V. Romano, W. Lüthy, Diam. Relat. Mater. **18**, 196 (2009)
10. M. Neff, T.V. Kononenko, S.M. Pimenov, V. Romano, W. Lüthy, V.I. Konov, Appl. Phys. A **97**, 543 (2009)
11. T.V. Kononenko, V.I. Konov, S.M. Pimenov, N.M. Rossukanyi, A.I. Rukovishnikov, V. Romano, Diam. Relat. Mater. **20**, 264–268 (2011)
12. S.M. Pimenov, I.I. Vlasov, A.A. Khomich, B. Neuenschwander, M. Muralt, V. Romano, Appl. Phys. A **105**, 673 (2011)
13. S.M. Pimenov, A.A. Khomich, I.I. Vlasov, E.V. Zavedeev, B. Neuenschwander, B. Jäggi, V. Romano, *ALT Proceedings*, vol. 1 (2012). doi:10.12684/alt.1.50
14. B. Caylar, M. Pomorski, P. Bergonzo, Appl. Phys. Lett. **103**, 043504 (2013)
15. A. Oh, B. Caylar, M. Pomorski, T. Wengler, Diam. Relat. Mater. **38**, 9 (2013)
16. T. Kononenko, V. Ralchenko, A. Bolshakov, V. Konov, P. Allegrini, M. Pacilli, G. Conte, E. Spiriti, Appl. Phys. A **114**, 297 (2014)
17. V.N. Strekalov, V.I. Konov, V.V. Kononenko, S.M. Pimenov, Appl. Phys. A **76**, 603 (2003)
18. S.M. Pimenov, B. Neuenschwander, B. Jäggi, V. Romano, Appl. Phys. A **114**, 1309 (2014)
19. R.H. Telling, C.J. Pickard, M.C. Payne, J.E. Field, Phys. Rev. Lett. **84**, 5160 (2000)
20. W.L. Mao, H. Mao, P.J. Eng, T.P. Trainor, M. Newville, C. Kao, D.L. Heinz, J. Shu, Y. Meng, R.J. Hemley, Science **302**, 425 (2003)
21. Q. Li, Y. Ma, A.R. Oganov, H. Wang, H. Wang, Y. Xu, T. Cui, H.-K. Mao, G. Zou, Phys. Rev. Lett. **102**, 175506 (2009)
22. J.-T. Wang, C. Chen, Y. Kawazoe, Phys. Rev. Lett. **106**, 075501 (2011)
23. M. Amsler, J.A. Flores-Livas, L. Lehtovaara, F. Balima, S. Alireza Ghasemi, D. Machon, S. Pailhès, A. Willand, D. Caliste, S. Botti, A. San Miguel, S. Goedecker, M.A.L. Marques, Phys. Rev. Lett. **108**, 065501 (2012)
24. Zh Li, F. Gao, Z. Xu, Phys. Rev. B **85**, 144115 (2012)
25. J.A. Flores-Livas, L. Lehtovaara, M. Amsler, S. Goedecker, S. Pailhès, S. Botti, A. San Miguel, M.A.L. Marques, Phys. Rev. B **85**, 155428 (2012)
26. S. Botti, M. Amsler, J.A. Flores-Livas, P. Ceria, S. Goedecker, M.A.L. Marques, Phys. Rev. B **88**, 014102 (2013)
27. K. Weingarten, Laser Tech. J. **6**(3), 51 (2009)
28. B. Neuenschwander, G.F. Bucher, C. Nussbaum, B. Joss, M. Muralt, U.W. Hunziker, P. Schuetz, Proc. SPIE **7584**, 75840R (2010)
29. www.e6cvd.com
30. I. Friel, S.I. Clewes, H.K. Dhillon, N. Perkins, D.J. Twitchen, G.A. Scarsbrook, Diam. Relat. Mater. **18**, 808 (2009)
31. R.P. Mildren, Intrinsic Optical Properties of Diamond, in *Optical Engineering of Diamond*, ed. by R.P. Mildren, J.R. Rabeau (Wiley-VCH Verlag GmbH & Co. KGaA, Weinheim, 2013)
32. A. Wotherspoon, J.W. Steeds, P. Coleman, D. Wolverson, J. Davies, S. Lawson, J. Butler, Diam. Relat. Mater. **11**, 692 (2002)
33. A.C. Ferrari, B. Kleinsorge, N.A. Morrison, A. Hart, V. Stolojan, J. Robertson, J. Appl. Phys. **85**, 7191 (1999)
34. T.V. Kononenko, A.A. Khomich, V.I. Konov, Diam. Relat. Mater. **37**, 50 (2013)
35. M.J. Matthews, M.A. Pimenta, G. Dresselhaus, M.S. Dresselhaus, M. Endo, Phys. Rev. B **59**, R6585 (1999)
36. A.C. Ferrari, J. Robertson, Phys. Rev. B **61**, 14095 (2000)
37. L.D. Landau, E.M. Lifshitz, *Theory of Elasticity* (Volume 7 of *A Course of Theoretical Physics*) (Pergamon Press, Oxford, 1970)
38. T.A. Friedmann, J.P. Sullivan, J.A. Knapp, D.R. Tallant, D.M. Follstaedt, D.L. Medlin, P.B. Mirkarimi, Appl. Phys. Lett. **71**, 3820 (1997)
39. A.C. Ferrari, J. Robertson, M.G. Beghi, C.E. Botani, R. Ferulano, R. Pastorelli, Appl. Phys. Lett. **75**, 1893 (1999)
40. H.O. Pierson, *Handbook of Carbon, Graphite, Diamond and Fullerenes (Properties, Processing and Applications)*, P.A. Thrower, Editor-in-Chief. (Noyes Publications, Park Ridge, 1993), p. 417
41. J.E. Field, C.S.J. Pickles, Diam. Relat. Mater. **5**, 625 (1996)
42. S. Prawer, R.J. Nemanich, Philos. Trans. R. Soc. Lond. A **362**, 2537 (2004)
43. M.H. Grimsditch, E. Anastassakis, M. Cardona, Phys. Rev. B **18**, 901 (1978)
44. J.M. Boteler, Y.M. Gupta, Phys. Rev. Lett. **71**, 3497 (1993)
45. I.I. Vlasov, V.G. Ralchenko, E.D. Obraztsova, A.A. Smolin, V.I. Konov, Appl. Phys. Lett. **71**, 1789 (1997)
46. E. Anastassakis, J. Appl. Phys. **86**, 249 (1999)
47. S.M. Pimenov, V.V. Kononenko, T.V. Kononenko, V.I. Konov, P. Fischer, V. Romano, H.P. Weber, A.V. Khomich, R.A. Khmelnitskiy, New Diam. Front. Carbon Technol. **14**(1), 21 (2004)
48. A. Tardieu, F. Cansell, J.P. Petitet, J. Appl. Phys. **68**, 3243 (1990)
49. P. Pavone, K. Karch, O. Shutt, W. Windl, D. Strauch, P. Giannozzi, S. Baroni, Phys. Rev. B **48**, 3156 (1993)
50. J.O. Orwa, K.W. Nugent, D.N. Jamieson, S. Prawer, Phys. Rev. B **62**, 5461 (2000)
51. O.N. Poklonskaya, A.A. Khomich, J. Appl. Spectrosc. **80**, 715 (2013)
52. A.V. Khomich, R.A. Khmelnitskii, X.J. Hu, A.A. Khomich, A.F. Popovich, I.I. Vlasov, V.A. Dravin, Y.G. Chen, A.E. Karkin, V.G. Ralchenko, J. Appl. Spectrosc. **80**, 707 (2013)